CELL BIOLOGY

# Superresolution and pulse-chase imaging reveal the role of vesicle transport in polar growth of fungal cells

Lu Zhou,[1,2] Minoas Evangelinos,[3,4,5] Valentin Wernet,[3] Antonia F. Eckert,[1] Yuji Ishitsuka,[1,6] Reinhard Fischer,[3] G. Ulrich Nienhaus,[1,2,6,7]* Norio Takeshita[3,8]*



**Polarized growth of filamentous fungi requires continuous transport of biomolecules to the hyphal tip. To this end, construction materials are packaged in vesicles and transported by motor proteins along microtubules and actin filaments. We have studied these processes with quantitative superresolution localization microscopy of live *Aspergillus nidulans* cells expressing the photoconvertible protein mEosFP*thermo* fused to the chitin synthase ChsB. ChsB is mainly located at the Spitzenkörper near the hyphal tip and produces chitin, a key component of the cell wall. We have visualized the pulsatory dynamics of the Spitzenkörper, reflecting vesicle accumulation before exocytosis and their subsequent fusion with the apical plasma membrane. Furthermore, high-speed pulse-chase imaging after photoconversion of mEosFP*thermo* in a tightly focused spot revealed that ChsB is transported with two different speeds from the cell body to the hyphal tip and vice versa. Comparative analysis using motor protein deletion mutants allowed us to assign the fast movements (7 to 10 μm $s^{-1}$) to transport of secretory vesicles by kinesin-1, and the slower ones (2 to 7 μm $s^{-1}$) to transport by kinesin-3 on early endosomes. Our results show how motor proteins ensure the supply of vesicles to the hyphal tip, where temporally regulated exocytosis results in stepwise tip extension.**

## INTRODUCTION

Polar growth is a general mechanism shared among a wide range of cell species, including epithelial cells with apical-basal polarity, migrating cells, and differentiating neurons (*1*, *2*). Likewise, filamentous fungi grow as highly polarized tubular cells, and their hyphal tip growth provides a convenient model system for polarized growth. Some filamentous fungi are pathogenic to animals and plants and invade their host cells via hyphal growth (*3*). Other fungi are used in biotechnology (for example, in enzyme production and fermentation in the food industry) because of their efficient enzyme secretion (*4*). Both pathogenicity and high secretion capability are closely connected to hyphal growth.

Polarized growth of fungal hyphae is sustained by the continuous delivery of vesicles loaded with biomolecules to the hyphal tips (*5*, *6*). In some filamentous fungi, these vesicles accumulate at the apices before fusion with the membrane. They form a structure called Spitzenkörper (*7*), which is thought to act as a vesicle supply center, a site where cargo for the hyphal tip is sorted (*8*). In the ascomycete filamentous fungus *Aspergillus nidulans*, microtubules extend all the way to the hyphal tip, whereas actin cables are found mostly near the hyphal tip (*9*). Vesicles containing components of the growth machinery are transported along microtubules from posterior sites to the apical region, transferred to actin cables, and finally delivered to the apical cortex of the hypha (*10*–*14*). These secretory vesicles (SVs) are released from the trans-Golgi network after maturation (*11*, *15*). Because gene deletion of kinesin-1 or myosin-5 decreases the amount of SVs at the hyphal tips, resulting in growth retardation, SVs are believed to be transported along microtubules by kinesin-1 and further along actin filaments by myosin-5 to the hyphal tip for exocytosis (*11*, *16*, *17*). However, localization analysis reported that kinesin-1 diffuses in the cytoplasm and myosin-5 accumulates at the hyphal tip (*17*, *18*). SV transport was not directly observed, probably due to the small size and fast motion. Early endosomes (EEs) are easier to track, so their bidirectional transport along microtubules by kinesin-3 and dynein has been thoroughly studied (*13*, *19*–*23*).

Filamentous fungi are covered by a cell wall consisting mainly of chitin and glucan. Thus, the synthesis of chitin, a β-1,4–linked homopolymer of *N*-acetylglucosamine, is essential for hyphal morphogenesis (*24*). Fungal chitin synthases are integral membrane proteins that have been classified into seven classes and three divisions according to their structural properties (*25*). Six chitin synthase genes have been isolated from *A. nidulans* (*26*). Among these, ChsB, a class III chitin synthase, is known to play a key role in hyphal tip growth, maintenance of cell wall integrity, and development (*27*). Class III chitin synthases are important for hyphal morphology, cell wall integrity, and pathogenicity in other filamentous fungi as well (*24*).

As yet, the molecular transport mechanism of cell wall–related enzymes including ChsB has largely remained elusive. Chitin synthases are thought to be transported on SVs to the plasma membrane for new cell wall synthesis, where they are subsequently internalized by endocytosis and transported on EEs for degradation in vacuoles, or recycled back to the plasma membrane (*28*). In previous work, we showed that kinesin-1 is required for transport of ChsB to the subapical region. However, mechanistic details could not be resolved due to high background fluorescence near the hyphal tip, insufficient time resolution to resolve fast motions, and the inability to distinguish between SVs and EEs (*29*). Here, we have used high-speed pulse-chase imaging as a powerful biophysical approach to analyze ChsB transport. Furthermore, we quantitatively studied the pulsatory dynamics of the Spitzenkörper and the associated stepwise hyphal growth by using superresolution localization imaging.

[1]Institute of Applied Physics, Karlsruhe Institute of Technology (KIT), Karlsruhe, Germany. [2]Institute of Nanotechnology, KIT, Karlsruhe, Germany. [3]Department of Microbiology, Institute for Applied Biosciences, KIT, Karlsruhe, Germany. [4]Faculty of Biology, University of Athens, Athens, Greece. [5]Institut de Biologie et de Médecine Moléculaires, Université Libre de Bruxelles, Gosselies, Belgium. [6]Department of Physics, University of Illinois at Urbana-Champaign, Urbana, IL 61801, USA. [7]Institute of Toxicology and Genetics, KIT, Eggenstein-Leopoldshafen, Germany. [8]Faculty of Life and Environmental Sciences, University of Tsukuba, Tsukuba, Japan.
*Corresponding author. Email: uli@uiuc.edu (G.U.N.); takeshita.norio.gf@u.tsukuba.ac.jp (N.T.)

## RESULTS

### Superresolution imaging and cluster analysis of the Spitzenkörper

ChsB localizes to hyphal tips and concentrates at the Spitzenkörper (*29*). To quantitatively analyze the spatiotemporal development of the Spitzenkörper with very high resolution, we imaged hyphae expressing ChsB as a fusion protein with mEosFP*thermo* (*30*), a thermostable, monomeric variant of the green-to-red photoconverting fluorescent protein EosFP (*31*, *32*) that is widely used for fluorescence imaging, pulse-chase experiments, and superresolution photoactivation localization microscopy (PALM) (*33*, *34*). Localization microscopy revealed a pronounced fluorescent cluster of mEosFP*thermo*-ChsB at the hyphal apex, representing the Spitzenkörper, and multiple speckles mostly near the plasma membrane (Fig. 1A).

ChsB clusters at the hyphal tip were identified by cluster analysis (*35*), as described in Materials and Methods (Fig. 1B). Cluster images of 2.5-s time intervals were generated for a total period of 125 s (Fig. 1C and movie S1) with a moving-window binning technique (500 frames binning with 50 frames shift, see Materials and Methods) (*36*), and cluster areas and numbers of mEosFP*thermo*-ChsB molecules within each cluster were calculated over the time course of the experiment (Fig. 1, D and E, and movie S2). In Fig. 1 (C to E), the dark green cluster of 0.1 $\mu m^2$ containing ~100 molecules is visible from 7.5 to 60 s. It grows via fusion with other clusters and evolves into the pink, crescent-shaped cluster of ~0.2 $\mu m^2$ containing ~200 molecules, visible from 62.5 to 80 s. Subsequently, this cluster breaks up into two smaller ones (~0.05 to 0.1 $\mu m^2$, ~50 to 100 molecules), depicted in light green and light blue. Overall, a total of 80 clusters were identified in this hyphal tip; their areas and numbers of molecules were calculated and compiled in histograms (Fig. 1, F and G). Markedly different cluster sizes were found because of fusion of small clusters or splitting of larger clusters over the time of the experiment. We have observed four subsets of cluster sizes, with average areas of 0.03 ± 0.01 $\mu m^2$ (red), 0.06 ± 0.01 $\mu m^2$ (blue), 0.11 ± 0.01 $\mu m^2$ (green), and 0.16 ± 0.01 $\mu m^2$ (pink); the overall average was 0.07 ± 0.04 $\mu m^2$. The corresponding average numbers of mEosFP*thermo*-ChsB molecules registered in the four subsets (Fig. 1E) were 20 ± 8 (red), 56 ± 7 (blue), 92 ± 17 (green), and 178 ± 12 (pink).

The shape change of the cluster from globular to crescent may signal the transition from vesicle accumulation before exocytosis to vesicle fusion with the apical plasma membrane during exocytosis. To test this hypothesis, we analyzed the temporal evolution of the apical cell edge from the PALM images in 20-s intervals (Fig. 1, H and I). Apparently, the extension rate of the hyphal tip varied over time; the largest displacements occurred from 50 to 70 s and from 90 to 110 s (Fig. 1I). These intervals coincide with those at which major changes of cluster

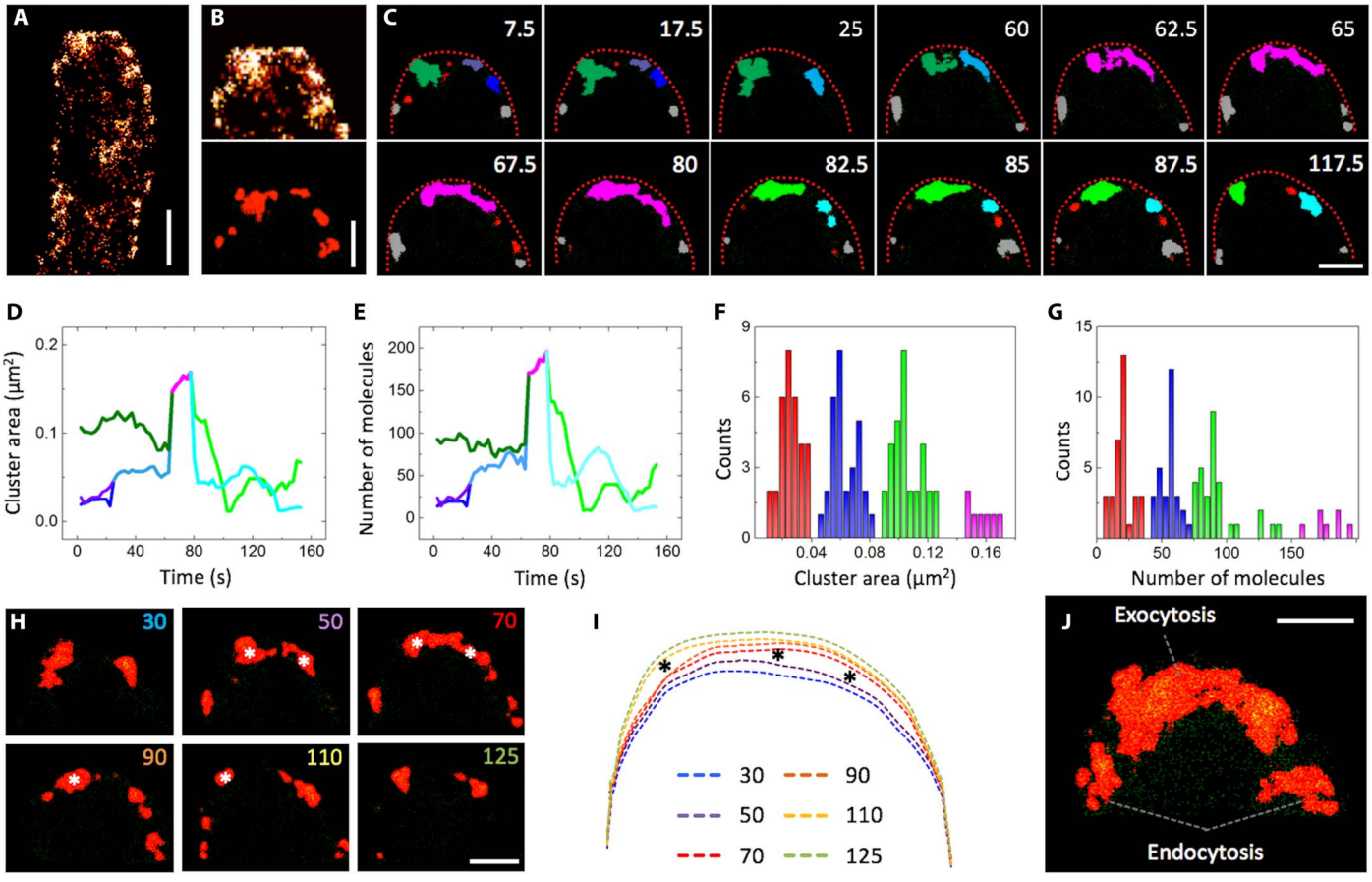


**Fig. 1. Superresolution imaging of Spitzenkörper dynamics.** (**A**) Localization image of a hypha with mEosFP*thermo*-ChsB clusters (500 frames). (**B**) Top: Image of the hyphal tip; bottom: ChsB clusters identified by cluster analysis. (**C**) Sequence of ChsB cluster images (clusters in different colors) rendered from images reconstructed by moving-window binning. (**D**) Time courses of total cluster areas. (**E**) Number of molecules. Lines are drawn in colors corresponding to the clusters in (C). Distributions of (**F**) cluster area and (**G**) number of molecules from all 80 identified clusters. (**H**) Sequence of images from cluster analysis. (**I**) Overlay of the corresponding tip profiles. Asterisks indicate large extensions of the apical membrane and shape change of the clusters. (**J**) Merged image of the image series in (H). Scale bars, 1 μm (A) and 300 nm (B, C, H, and J).

shapes (Fig. 1H, 50 to 70 s) and a reduction of cluster size (90 to 110 s) are observed. These results reveal that SVs accumulate at the Spitzenkörper during the slow growth phase. Then, they fuse with the plasma membrane and spur fast growth.

In addition to the crescent domain along the apical membrane, there are also two separate subapical domains in the merged image from the entire time sequence (Fig. 1J). This result supports previous work reporting that endocytosis occurs in an annular structure around the hyphal tube, spatially separated from the hyphal apex where SVs are delivered for exocytosis (*37*).

### Pulse-chase analysis of mEosFP*thermo*-ChsB after photoconversion 5 μm from the hyphal tip

We used high-speed pulse-chase imaging of mEosFP*thermo*-ChsB after photoconversion to monitor its transport. After photobleaching all red-emitting molecules with a 561-nm laser, we irradiated a spot ~5 μm behind the hyphal tip for 1 s with a tightly focused 405-nm laser beam to locally photoconvert mEosFP*thermo*-ChsB to its red-emitting form (see Materials and Methods). In Fig. 2A, image "0" shows the red fluorescence excited by the 405-nm laser, marking the local photoconversion spot. Then, the 561-nm laser was again switched on (Fig. 2A, image "1"), and images were acquired for 15 to 30 s with a dwell time of 50 ms (Fig. 2A and movie S3). A large red-emitting spot appeared at the site of photoconversion, which gradually faded and dispersed due to vesicle transport away from the photoconversion region. By taking advantage of the low background in this pulse-chase imaging scheme, both anterograde (from back to tip) and retrograde (from tip to back) vesicle movements are easily observed in a kymograph along the axis of the hypha (Fig. 2B). The typical linear vesicle displacements were occasionally interrupted by brief

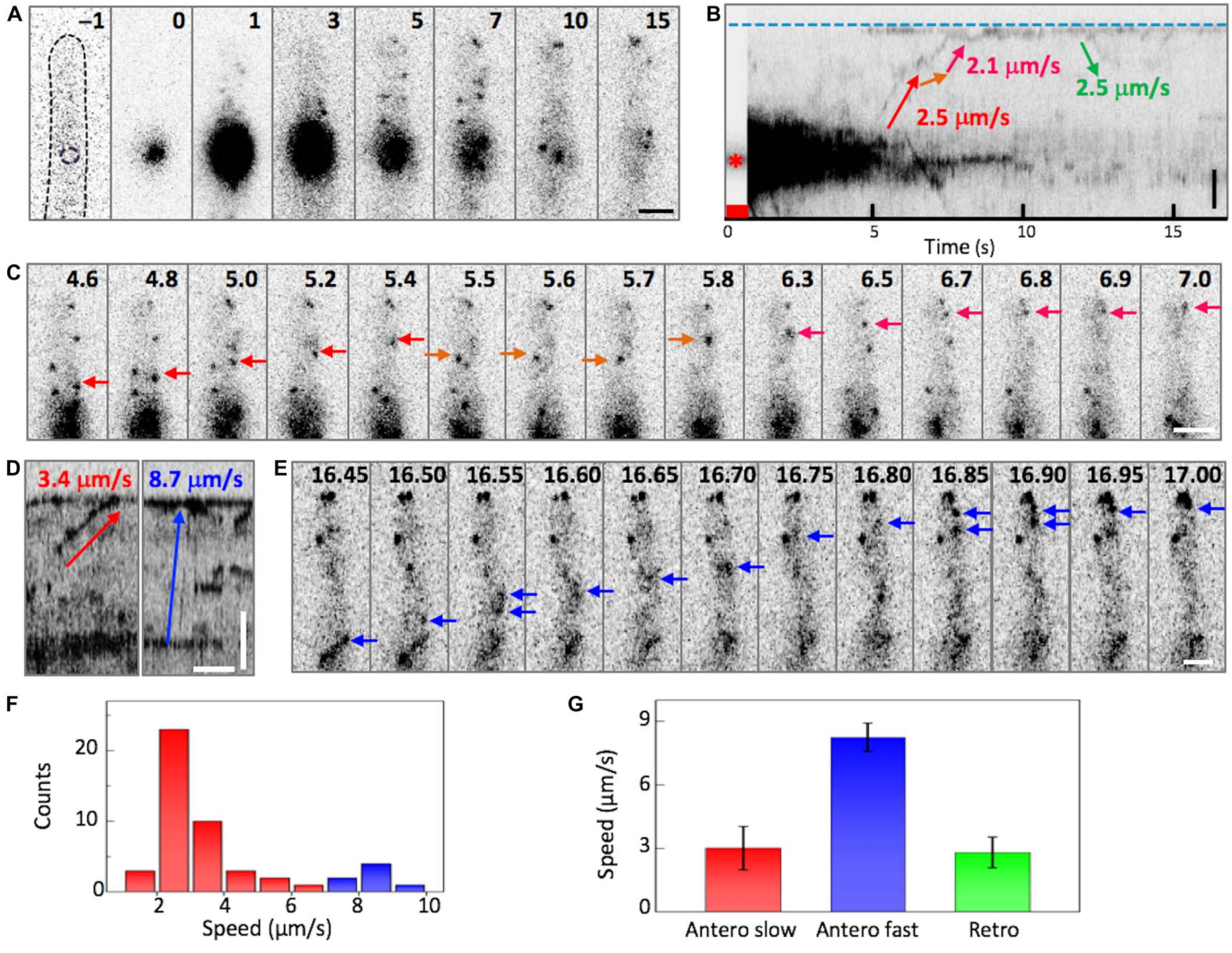


**Fig. 2. Pulse-chase analysis of mEosFP*thermo*-ChsB in the hyphal tip region.** (**A**) Images of mEosFP*thermo*-ChsB before photoconversion (−1), with 405-nm light applied at the spot marked by the dashed line for 1 s (0) and after photoconversion. (**B**) Kymograph calculated from (A); arrows indicate anterograde and retrograde transport. The blue dashed line and the red asterisk mark the positions of the hyphal tip and the photoconversion locus, respectively; the red square indicates the photoconversion interval. (**C**) Image sequence from 4.6 to 7 s after photoconversion; arrows mark the transport processes in (B) in corresponding colors. (**D**) Kymographs of slow (red) and fast (blue) transport of mEosFP*thermo*-ChsB. Vertical scale bar, 2 μm; horizontal scale bar, 1 s. (**E**) Image sequences of the fast transport process marked by the blue arrow in (D) observed from 16.45 to 17 s. (**F**) Speed distribution of anterograde transport. (**G**) Speed of slow anterograde (red), fast anterograde (blue), and retrograde (green) transport (mean ± SD; $n$ = 42, 7, and 9, respectively). Scale bars, 2 μm. The elapsed time is given in seconds.

stops (Fig. 2, B and C), and there were also some immobile spots. We further noticed that the fluorescence from the hyphal tip stayed constant beyond ~5 s after photoconversion (Fig. 2B).

The slopes of the lines in the kymograph encode the speed of ChsB vesicle movement. From observations of a large number of hyphae, we noticed that most displacements occurred at speeds of 2 to 4 μm $s^{-1}$; however, there were also clearly faster processes with speeds of 7 to 10 μm $s^{-1}$ (Fig. 2, D and E). Accordingly, the speed histogram of anterograde movements in Fig. 2F appears to consist of two subdistributions, a predominant distribution below ~7 μm $s^{-1}$ associated with slow transport centered on 3.0 ± 1.0 μm $s^{-1}$ (mean ± SD; $n$ = 42) and a smaller distribution above ~7 μm $s^{-1}$ representing fast transport centered on 8.3 ± 0.7 μm $s^{-1}$ (mean ± SD; $n$ = 7) (Fig. 2, F and G, red and blue, respectively). Retrograde transport was less frequent (15% of events, $n$ = 9); its average speed was 2.9 ± 0.8 μm $s^{-1}$ and thus within the error identical to that of slow anterograde transport (Fig. 2G).

To further investigate the two putative types of transport, we measured the transport speed of green fluorescent protein (GFP)–RabA, a marker of EEs (*20*). Anterograde and retrograde vesicle movements are visible in a kymograph along the hyphal axis, with identical speeds of 2.0 ± 0.5 μm $s^{-1}$ (mean ± SD; $n$ = 76 and 62, respectively; fig. S1, A and B, and movie S4). We also performed the pulse-chase experiment on hyphae expressing mEosFP*thermo*-TeaR (fig. S1C), a fusion protein containing the membrane-associated polarity marker TeaR known to be transported on SVs (*36*, *38*). Here, we found significantly more fast transport events than with mEosFP*thermo*-ChsB, with average speeds of 7.9 ± 3.6 μm $s^{-1}$ for anterograde movements (mean ± SD; $n$ = 95) and 8.3 ± 3.8 μm $s^{-1}$ for retrograde movements (mean ± SD; $n$ = 87) (fig. S1, B and C, and movie S5). Notably, the average speeds of slow transport of mEosFP*thermo*-ChsB and GFP-RabA and of fast transport of mEosFP*thermo*-ChsB and mEosFP*thermo*-TeaR are identical within the error (fig. S1D), and the histograms of the individual events are similar as well (fig. S1D). In a strain coexpressing GFP-ChsB and mCherry-RabA, we observed that GFP-ChsB partially comigrates with mCherry-RabA (fig. S1E and movie S6). These results strongly suggest that slow and fast transport events of ChsB represent ChsB on EEs and SVs, respectively.

### Pulse-chase analysis using microtubule or actin cytoskeleton–destabilizing drugs

We performed the pulse-chase experiment on hyphae treated with either benomyl (2 μg/ml), a microtubule-destabilizing drug (*39*), or cytochalasin A (2 μg/ml), an F-actin–destabilizing drug (*9*), for 5 to 30 min before imaging. In the presence of benomyl, there were mostly immobile spots near the photoconversion locus (fig. S2, A to E, and movie S7); anterograde and retrograde transport events were rarely visible in comparison to the control (fig. S2, D and F). We also did not find any mEosFP*thermo*-ChsB accumulation at the hyphal tips (fig. S2A), and the signal intensity at the photoconversion locus persisted longer than in the control (fig. S2B). All these findings indicate that SV transport is suppressed.

In contrast, both anterograde and retrograde transport events were found upon application of cytochalasin A (fig. S2, G to I, and movie S8). However, in marked contrast to the control, vesicles reaching the hyphal tip did not stay there but were immediately reflected backward (fig. S2I). As a result, there was no stable ChsB signal from the hyphal tips (fig. S2A) and more frequent retrograde transport (fig. S2F). These data show that F-actin is required at the hyphal tip to accept SVs transported along microtubules and to guide them to the sites of exocytosis (*11*).

### Pulse-chase analysis using kinesin-1, kinesin-3, and myosin-5 deletion strains

We further performed pulse-chase experiments with *kinA* (kinesin-1), *uncA* (kinesin-3), or *myoV* (myosin-5) deletion strains. In the *kinA* deletion strain, spots remained immobile after photoconversion, as with benomyl treatment, and neither transport nor signal accumulation at the hyphal tips was observed (Fig. 3, A and D, and movie S9). These findings support the common view that KinA transports SVs over long distance along microtubules to hyphal tips (*11*, *29*).

In the *uncA* deletion strain, the red fluorescence generated by photoconversion spreads markedly faster than in the wild type, and fast transport events in both directions were more frequently observed in the kymograph in comparison to the wild type (Fig. 3, B and E, and movie S10), with average speeds of 8.3 ± 2.0 μm $s^{-1}$ for anterograde motion (mean ± SD; $n$ = 44) and 8.6 ± 3.1 μm $s^{-1}$ for retrograde motion (mean ± SD; $n$ = 51) (Fig. 3F). These values are identical within the error to the speed of fast transport in the wild type (Fig. 3G). Some spots reached the hyphal tip but immediately reverted, so there was no accumulation at the tip (Fig. 3, B and D). Because kinesin-3 (UncA) transports EEs (*13*, *21*, *23*), the absence of slow transport in the *uncA* deletion strain further strengthens our assignment of fast and slow ChsB transport to movement on SVs and EEs, respectively.

MyoV is believed to transport SVs along actin cables for exocytosis at the hyphal tip (*10*, *17*, *40*). Consequently, the *myoV* deletion strain has severe growth defects. Similar to the *uncA* deletion strain, the *myoV* deletion strain showed faster spreading of red fluorescence after photoconversion than the wild type (Fig. 3C and movie S11). There were significantly more fast transport events than for the wild type (Fig. 3E), with average speeds of 7.2 ± 2.9 μm $s^{-1}$ for anterograde motion (mean ± SD; $n$ = 46) and 5.9 ± 2.6 μm $s^{-1}$ for retrograde motion (mean ± SD; $n$ = 38) (Fig. 3, F and G). Similar to the wild type treated with cytochalasin A, spots reaching the hyphal tip did not accumulate there but immediately moved backward (Fig. 3D). Together, these data indicate that both MyoV and actin cables are required for capturing SVs transported along microtubules at the hyphal tip.

In the pulse-chase experiments performed with the *uncA* and *myoV* deletion strains, the number of locally photoconverted mEosFP*thermo*-ChsB is increased by 46% and 40% with respect to the wild type (fig. S3, A to D). These observations could, in principle, be explained by variations in the expression levels of *chsB* among the strains. These are, however, of comparable magnitude within the error (fig. S3E). Alternatively, faster vesicle dynamics in the *uncA* and *myoV* deletion strains could result in more mEosFP*thermo*-ChsB transiting the irradiated region during photoconversion. The fraction of fast-moving SVs on microtubules is greater in these two motor mutants because of their impairment of SV supply to the hyphal tip.

### Pulse-chase analysis after photoconversion at the hyphal tip

We next irradiated a spot at the hyphal tip for 1 s with 405-nm light to induce local green-to-red photoconversion, and imaged the tagged ChsB molecules for 30 s with a dwell time of 50 ms (Fig. 4A and movie S12). A large spot appeared at the hyphal tip right after photoconversion and gradually shrank and dispersed, accompanied by smaller spots moving away. We performed this experiment also on hyphae treated with benomyl or cytochalasin A, and in the *uncA* deletion strain (Fig. 4, B to D).

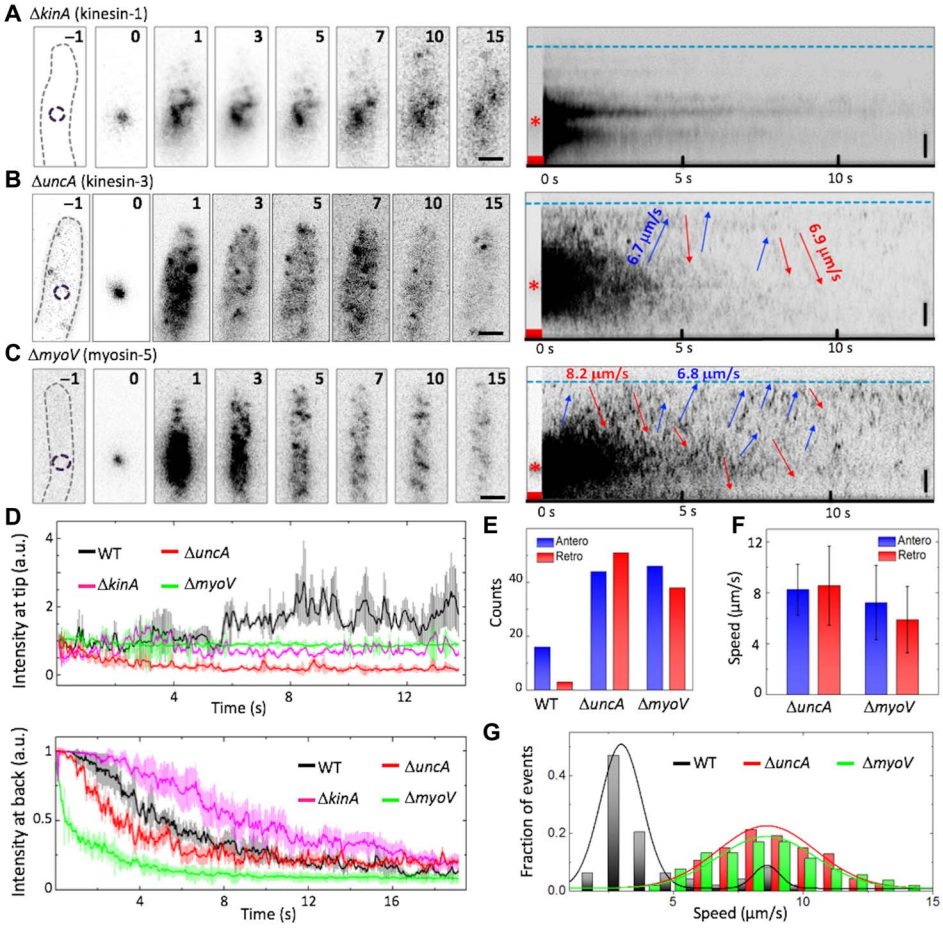


**Fig. 3. Pulse-chase analysis of mEosFP*thermo*-ChsB in the hyphal tip regions of cells from motor mutants.** (**A** to **C**) Left: Image sequence upon photoconversion at $t = 0$ s for 1 s in a spot ~5 μm behind the hyphal tip (dashed circles in panels "−1") of (A) Δ*kinA*, (B) Δ*uncA*, and (C) Δ*myoV*. The elapsed time is given in seconds. Scale bars, 2 μm. Right: Corresponding kymographs; arrows indicate anterograde (blue) and retrograde (red) transport. Blue dashed lines and asterisks mark the positions of hyphal tips and photoconversion loci, respectively; red squares indicate the photoconversion intervals. Vertical scale bars, 2 μm. (**D**) Fluorescence intensities at (top) hyphal tips and (bottom) photoconversion loci from wild-type (WT) (black), Δ*kinA* (green), Δ*uncA* (red), and *myoV* (green) cells, averaged and plotted as mean ± SD ($n = 3$ to 5). (**E**) Number of anterograde (blue) and retrograde (red) transport events in six kymographs of WT, Δ*uncA*, and Δ*myoV*. (**F**) Speed of anterograde (blue) and retrograde (red) transport in Δ*uncA* and Δ*myoV* (mean ± SD). (**G**) Distribution of speeds in anterograde transport from WT (black), Δ*uncA* (red), and Δ*myoV* (green) samples. a.u., arbitrary units.

The tagged ChsB molecules at the hyphal apex moved to subapical patches and presumably internalized there (fig. S4A, green arrows). We found both anterograde and retrograde transport events (Fig. 4E). The anterograde fluorescence signals from the tip remained close to the plasma membrane, merged with signals from the subapical patches, and moved further backward together (fig. S4A, red arrows). Overall, 60% of the transport events were retrograde and 40% were anterograde (Fig. 4F). Because the average speeds of anterograde and retrograde transport events were ~2 to 3 μm $s^{-1}$ (Fig. 4G), we assign both to ChsB transport on EEs along microtubules.

After benomyl treatment (2 μg/ml) for 5 to 30 min before imaging, a large fraction of ChsB was found near the hyphal tip but not at the apical membrane (Fig. 4, B and H; fig. S4B; and movie S13). Moreover, ChsB transport essentially ceased (Fig. 4F), so we conclude that microtubules are dispensable for ChsB endocytosis but necessary for ChsB transport away from the tip region. After cytochalasin A treatment (2 μg/ml) for 5 to 30 min before imaging, ChsB was found at the apical membrane. The signal intensity was lower than in the control but stayed at the apical membrane, where it gradually faded (Fig. 4, C and H; fig. S4B; and movie S14); transport events were hardly detected (Fig. 4F). These results show that an intact actin cytoskeleton is crucial for ChsB endocytosis and its transport away from the tip region. In the *uncA* deletion strain, the ChsB fluorescence spread faster from the hyphal tip than in the wild type (Fig. 4D and movie S15); both anterograde and retrograde transport events were observed more frequently (Fig. 4I). Moreover, the average speeds of anterograde and retrograde transport events were 8.0 ± 1.8 μm $s^{-1}$ and 7.7 ± 2.4 μm $s^{-1}$ (mean ± SD; $n = 41$ and 43, respectively) (Fig. 4G). These fast speeds suggest that ChsB in the *uncA* deletion strain is transported in both directions mainly on SVs along microtubules.

## DISCUSSION

By using superresolution microscopy, we observed that the SVs carrying ChsB are not evenly supplied along the apical membrane but rather in clusters, and the Spitzenkörper forms by fusion of these

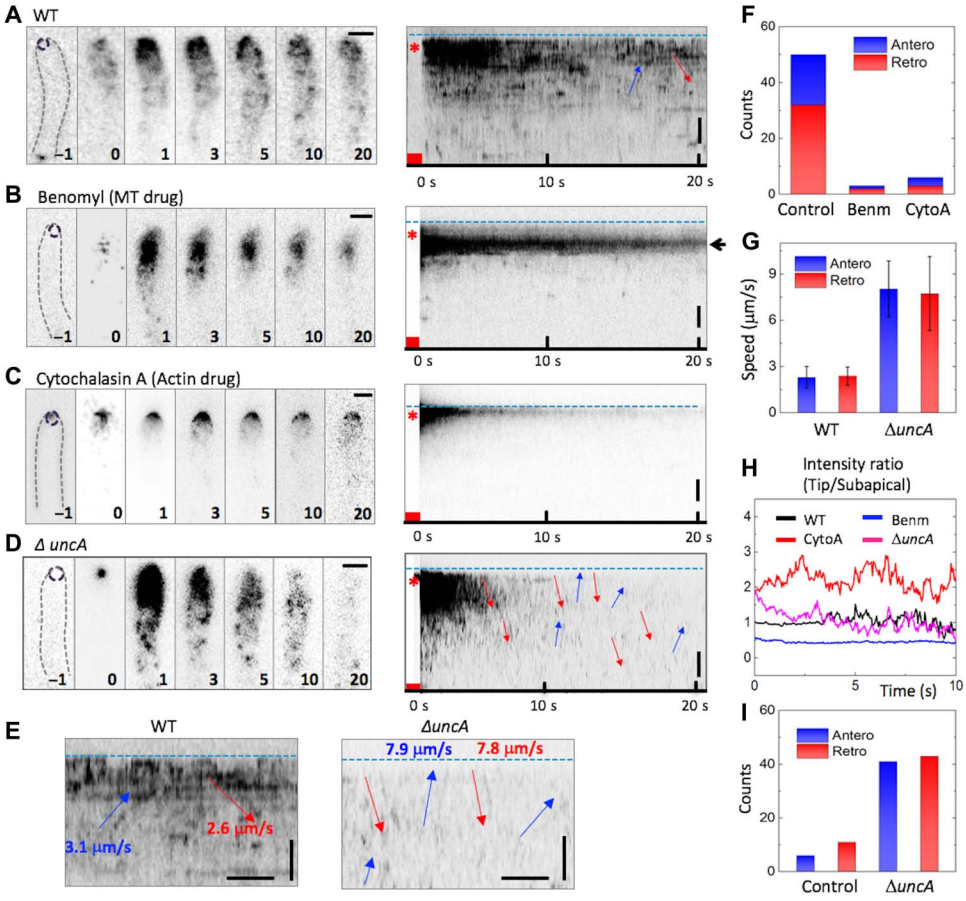


**Fig. 4. Pulse-chase analysis after mEosFP*thermo*-ChsB photoconversion at the hyphal tip.** (**A** to **D**) Left: Image sequences upon photoconversion at $t = 0$ s for 1 s at the hyphal tips (dashed circles in panels "−1") of (A) a WT cell without drugs (as a control) and in the presence of (B) benomyl (Benm), (C) cytochalasin A (CytoA), and (D) a cell from the Δ*uncA* strain. The elapsed time is given in seconds. Right: Corresponding kymographs; blue dashed lines and asterisks mark the positions of hyphal tips and photoconversion loci, respectively; red squares indicate the photoconversion intervals. (**E**) Enlarged kymographs of WT (left) and Δ*uncA* (right) cells; vertical scale bar, 2 μm; horizontal scale bar, 1 s. Arrows show anterograde (blue) and retrograde (red) transport events; blue dashed lines indicate the hyphal tip positions. (**F**) Number of anterograde (blue) or retrograde (red) transport events in 20 kymographs of the control, with benomyl, and with cytochalasin A. (**G**) Speeds of anterograde (blue) and retrograde (red) transport in WT and Δ*uncA* (mean ± SD). (**H**) Time courses of signal intensity ratio between hyphal tip area and subapical area from a WT cell without drugs (control) and in the presence of benomyl or cytochalasin A, and in the Δ*uncA* strain. Further details are given in fig. S3. (**I**) Number of anterograde (blue) or retrograde (red) transport events from five kymographs of WT and Δ*uncA* cells. MT, microtubule.

clusters. Transient formation of local hotspots along the apical membrane has also been found for the polarity marker TeaR (*36*). We observed a characteristic shape change of the Spitzenkörper from globular to crescent that was accompanied by enhanced membrane extension. Apparently, SVs accumulate at the Spitzenkörper during phases of slow growth and then fuse with the plasma membrane, generating bursts of fast growth. Afterward, the material is depleted and needs to be replenished. These findings provide further support to our recently proposed "transient polarity assembly model" (*36*). This stepwise growth of hyphal tips was shown in several filamentous fungi (*41*), and a shape change of the Spitzenkörper correlated with the growth rate in another fungus (*42*). Recently, we reported that pulsatory $Ca^{2+}$ influx controls actin polymerization and exocytosis, resulting in stepwise cell extension (*43*). This characteristic intermittent growth may enable cells to respond more rapidly to chemical or mechanical cues.

Local photoconversion of mEosFP*thermo*-ChsB allowed us to tag a small subset of molecules at an arbitrary location in the cell and trace their movement with exceptionally low background fluorescence by using high-speed pulse-chase imaging. We showed that ChsB is transported from the cell body to the hyphal tip or vice versa with two different speeds, that is, below and above ~7 μm $s^{-1}$. By comparison with the transport of EE and SV markers, we were able to assign the slow and fast transport unambiguously to ChsB associated with EEs and SVs, respectively. To the best of our knowledge, this is the first time that fast transport of SVs was directly observed in filamentous fungi. In fungi, EEs are four to five times larger than SVs (*44*, *45*). Therefore, the slower transport of EEs is probably caused by the size of the cargo. Notably, in cultured mammalian cells, the speeds of kinesin-1 and kinesin-3 are similar (~1 to 2 μm $s^{-1}$) (*46*, *47*). A schematic depiction of the ChsB transport mechanism in the wild-type strain is shown in Fig. 5.

The experiments involving cytoskeleton-destroying drugs revealed that ChsB molecules are transported on microtubules to the hyphal tip, where they continue on actin cables to the sites of exocytosis (*11*). A complementary approach to understand vesicle transport is the use of deletion strains that do not express the motor proteins moving cargo along these cytoskeletal structures. The markedly dif-

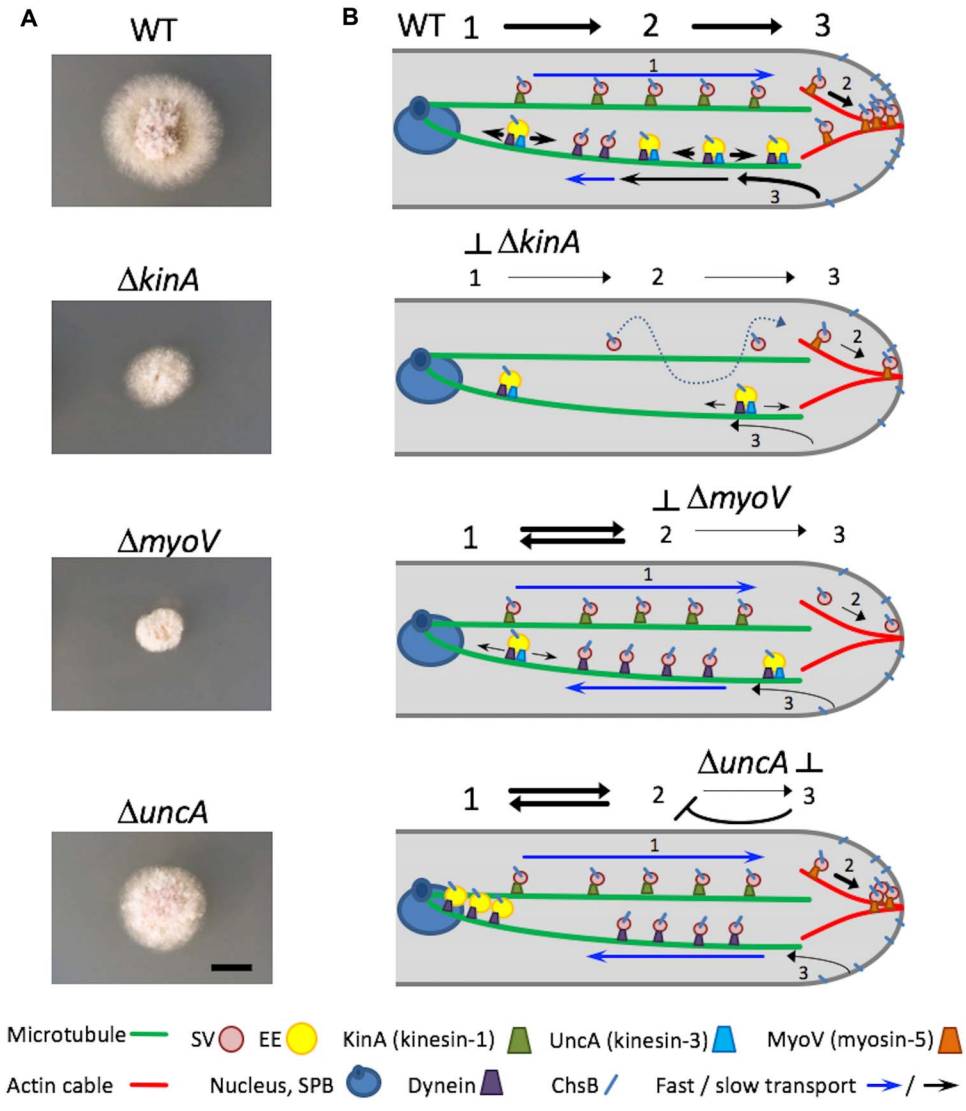


**Fig. 5. Images of fungal colonies and schematic depictions of ChsB transport in WT, Δ*kinA*, Δ*myoV*, and Δ*uncA* strains.** (**A**) Images of the colonies; scale bar (for all images), 5 mm. Strains were grown on the same minimal medium glucose agar plate for 2 days. (**B**) Depictions of ChsB transport processes in the four strains (for details, see the text); the symbol legend is included below. SPB, spindle pole body.

ferent growth of wild-type, Δ*kinA*, Δ*uncA*, and Δ*myoV* strains attests to the essential role of these motor proteins in sustaining polar growth (Fig. 5A). Kinesin-1 is required for transport of SVs over long distances along microtubules to hyphal tips (*29*). Without KinA, active transport of SVs ceases; only diffusion can still occur and polar growth is strongly impaired (Fig. 5). The *myoV* deletion strains displayed fast transport of ChsB in both directions, but there was no signal accumulation at the tip. Myosin-5 is thought to move along actin cables and carry SVs to the sites of exocytosis (*17*). Without actin cables and/or myosin-5, SVs cannot be captured at the tip and are immediately reflected, resulting in circular transport of SVs in both directions with a microtubule-based conveyor belt (Fig. 5B) (*11*, *48*). The impaired exocytosis gives rise to severe growth defects (Fig. 5A). Notably, we only rarely observed ChsB transport on EEs after endocytosis because only very little ChsB arrived at the hyphal tips.

In the *uncA* deletion strain, ChsB was transported at high speed in both directions but did not accumulate at the hyphal tip. Because kinesin-3 transports EEs (*13*, *21*, *23*), the absence of slow transport in the *uncA* deletion strain suggests that ChsB is transported predominantly by kinesin-1 on fast-moving SVs (Fig. 5B). Although myosin-5 is present, the SVs are not captured at the hyphal tip. Because kinesin-3 and dynein are assumed to transport EEs bidirectionally along microtubules in the recycling pathway, deletion of kinesin-3 suppresses this transport branch. The machinery becomes clogged with EEs at the minus end of microtubules located at the spindle pole body on the nuclei. Because the supply of SVs for exocytosis is regulated by the balance of exocytosis and endocytosis, the putative endocytosis defect in the kinesin-3 mutant might affect exocytosis and cause circular transport of SVs. This hypothesis is supported by the lower growth rate of the kinesin-3 mutant with respect to the wild-type strains, but it is still higher than for the kinesin-1 or myosin-5 deletion strains (Fig. 5A).

To conclude, by using advanced quantitative optical imaging, we have elucidated how motor proteins ensure the supply of vesicles to

the hyphal tip, where temporally regulated exocytosis results in stepwise extension of the fungal tip. We believe that these new insights will be beneficial for the development of fungal-based biotechnology applications in fields such as food science, agriculture, pharmacology, and medicine.

## MATERIALS AND METHODS

### Strains, plasmids, and culture conditions

A list of *A. nidulans* strains used in this study was given in table S1. The sequence of *chsB* is amplified from genomic DNA by using the primers 5′-cggcgcgcctATGGCCTACCACGGCTC-3′ (chsB_Asc I_fwd) and 5′-cttaattaattaGGCAACACACTGACATATCC-3′ (chsB_Pac I_rev). The Asc I–Pac I–digested *chsB* sequence was replaced with the *teaR* sequence in pNT65 (for mEosFP*thermo* tagging at the N terminus of *teaR* expressed under the regulatable *alcA* promoter; contains *pyr-4*) (*36*), yielding pNT75. The plasmids were transformed into the TN02A3 strain (*ku70* deletion) (*48*), yielding SNT167. SNT167 (mEosFP*thermo*-ChsB) was crossed with SNZ9 (Δ*uncA*) (*21*), selected, and designated as SNT169 (mEosFP*thermo*-ChsB, Δ*uncA*). SNR1 (Δ*kinA*) and SRM89 (Δ*myoV*) (*49*) were transformed with pNT75 and pI4 (*pyroA* marker), yielding SNT168 (mEosFP*thermo*-ChsB, Δ*kinA*) and SNT170 (mEosFP*thermo*-ChsB, Δ*myoV*). Supplemented minimal medium for *A. nidulans* and standard strain construction procedures were described previously (*50*). All cells were cultured in minimal medium supplemented with 2% glycerol as carbon source (*alcA* promoter derepressive condition). The expression of mEosFP*thermo*-ChsB under the inducible *alcA* promoter instead of native ChsB did not show any abnormal phenotype. Cells were incubated at 28°C overnight in a chambered cover glass (Thermo Fisher Scientific). Benomyl and cytochalasin A (Sigma) were used as described previously (*38*).

### Live-cell imaging

PALM images were acquired at room temperature on a modified inverted microscope (Axiovert 200, Zeiss), as described previously (*36*). The fluorescent protein mEosFP*thermo* was photoconverted from its green- to its red-emitting form by a 405-nm laser at low intensity and simultaneously excited by a 561-nm laser. Molecule localization analyses were carried out using a-livePALM (*35*), a custom-written analysis software. For cluster analysis (*36*), molecules from 500 continuous frames (25 s) were collected and analyzed. For each molecule, we computed the number of detected neighboring molecules within 50-nm distance. If one molecule had more than 10 neighboring molecules, then the pixel was considered as a cluster pixel. Adjacent cluster pixels were defined as belonging to the same cluster. For details, see the Supplementary Materials.

For pulse-chase experiments, the whole cell was first prebleached by strong 561-nm laser irradiation (0.8 to 1 kW/cm$^2$), followed by irradiation with a tightly focused 405-nm laser for 1 s, either at the tip or in the body region of the cell to locally photoconvert a small number of mEosFP*thermo*-ChsB molecules. Then, the 561-nm laser was switched on again (200 to 400 W/cm$^2$) to excite the red-emitting mEosFP*thermo*-ChsB molecules. Images were processed by ImageJ.

## SUPPLEMENTARY MATERIALS

Supplementary material for this article is available at http://advances.sciencemag.org/cgi/content/full/4/1/e1701798/DC1

Supplementary Materials and Methods

fig. S1. Transport of EEs and SVs.

fig. S2. Pulse-chase analysis of mEosFP*thermo*-ChsB near the hyphal tip in the presence of microtubule or actin-depolymerizing drugs.

fig. S3. Quantitative analysis of mEosFP*thermo*-ChsB numbers in the hyphal tip and expression levels.

fig. S4. Pulse-chase analysis upon mEosFP*thermo*-ChsB photoconversion at the hyphal tip.

movie S1. Superresolution movie of mEosFP*thermo*-ChsB clusters generated with the moving-window binning technique (500 frames binning with 50 frames shift).

movie S2. Dynamics of ChsB clusters identified by cluster analysis.

movie S3. Pulse-chase imaging of mEosFP*thermo*-ChsB in the wild-type hyphal tip region with local photoconversion ~5 μm behind the hyphal tip.

movie S4. Transport of EEs.

movie S5. Pulse-chase imaging of mEosFP*thermo*-TeaR in the wild-type hyphal tip region with a local photoconversion ~5 μm behind the hyphal tip.

movie S6. Partial comigration of GFP-ChsB and mCherry-RabA.

movie S7. Pulse-chase imaging of mEosFP*thermo*-ChsB near the hyphal tip in the presence of microtubule drugs (benomyl, 2 μg/ml).

movie S8. Pulse-chase imaging of mEosFP*thermo*-ChsB near the hyphal tip in the presence of actin-depolymerizing drugs (cytochalasin A, 2 μg/ml).

movie S9. Pulse-chase imaging of mEosFP*thermo*-ChsB in the hyphal tip region of the cell from the *kinA* deletion strains.

movie S10. Pulse-chase imaging of mEosFP*thermo*-ChsB in the hyphal tip region of the cell from the *uncA* deletion strains.

movie S11. Pulse-chase imaging of mEosFP*thermo*-ChsB in the hyphal tip region of the cell from the myoV deletion strains.

movie S12. Pulse-chase imaging after mEosFP*thermo*-ChsB photoconversion at the hyphal tip of a wild-type cell.

movie S13. Pulse-chase imaging after mEosFP*thermo*-ChsB photoconversion at the hyphal tip in the presence of microtubule drugs (benomyl, 2 μg/ml).

movie S14. Pulse-chase imaging after mEosFP*thermo*-ChsB photoconversion at the hyphal tip in the presence of actin-depolymerizing drugs (cytochalasin A, 2 μg/ml).

movie S15. Pulse-chase imaging after mEosFP*thermo*-ChsB photoconversion at the hyphal tip of a cell from the *uncA* deletion strain.

table S1. *A. nidulans* strains used in this study.

Reference (*51*)

## REFERENCES AND NOTES


1. N. W. Goehring, S. W. Grill, Cell polarity: Mechanochemical patterning. *Trends Cell Biol.* **23**, 72–80 (2013).
2. W. J. Nelson, Adaptation of core mechanisms to generate cell polarity. *Nature* **422**, 766–774 (2003).
3. C. Garcia-Vidal, D. Viasus, J. Carratalà, Pathogenesis of invasive fungal infections. *Curr. Opin. Infect. Dis.* **26**, 270–276 (2013).
4. P. J. Punt, N. van Biezen, A. Conesa, A. Albers, J. Mangnus, C. van den Hondel, Filamentous fungi as cell factories for heterologous protein production. *Trends Biotechnol.* **20**, 200–206 (2002).
5. W. R. Rittenour, H. Si, S. D. Harris, Hyphal morphogenesis in *Aspergillus nidulans*. *Fungal Biol. Rev.* **23**, 20–29 (2009).
6. P. E. Sudvery, Regulation of polarized growth in fungi. *Fungal Biol. Rev.* **22**, 44–55 (2008).
7. S. D. Harris, The Spitzenkörper: A signalling hub for the control of fungal development? *Mol. Microbiol.* **73**, 733–736 (2009).
8. M. Riquelme, E. Sánchez-León, The Spitzenkörper: A choreographer of fungal growth and morphogenesis. *Curr. Opin. Microbiol.* **20**, 27–33 (2014).
9. A. Bergs, Y. Ishitsuka, M. Evangelinos, G. U. Nienhaus, N. Takeshita, Dynamics of actin cables in polarized growth of the filamentous fungus *Aspergillus nidulans*. *Front. Microbiol.* **7**, 682 (2016).
10. N. Taheri-Talesh, T. Horio, L. Araujo-Bazán, X. Dou, E. A. Espeso, M. A. Peñalva, S. A. Osmani, B. R. Oakley, The tip growth apparatus of *Aspergillus nidulans*. *Mol. Biol. Cell* **19**, 1439–1449 (2008).
11. A. Pantazopoulou, M. Pinar, X. Xiang, M. A. Peñalva, Maturation of late Golgi cisternae into RabE$^{RAB11}$ exocytic post-Golgi carriers visualized in vivo. *Mol. Biol. Cell* **25**, 2428–2443 (2014).
12. R. Fischer, N. Zekert, N. Takeshita, Polarized growth in fungi—Interplay between the cytoskeleton, positional markers and membrane domains. *Mol. Microbiol.* **68**, 813–826 (2008).
13. M. J. Egan, K. Tan, S. L. Reck-Peterson, Lis1 is an initiation factor for dynein-driven organelle transport. *J. Cell Biol.* **197**, 971–982 (2012).
14. N. Takeshita, R. Manck, N. Grün, S. H. de Vega, R. Fischer, Interdependence of the actin and the microtubule cytoskeleton during fungal growth. *Curr. Opin. Microbiol.* **20**, 34–41 (2014).
15. M. Pinar, H. N. Arst Jr., A. Pantazopoulou, V. G. Tagua, V. de los Ríos, J. Rodríguez-Salarichs, J. F. Díaz, M. A. Peñalva, TRAPPII regulates exocytic Golgi exit by mediating nucleotide exchange on the Ypt31 ortholog RabE$^{RAB11}$. *Proc. Natl. Acad. Sci. U.S.A.* **112**, 4346–4351 (2015).

16. S. Seiler, F. E. Nargang, G. Steinberg, M. Schliwa, Kinesin is essential for cell morphogenesis and polarized secretion in *Neurospora crassa*. *EMBO J.* **16**, 3025–3034 (1997).
17. N. Taheri-Talesh, Y. Xiong, B. R. Oakley, The functions of myosin II and myosin V homologs in tip growth and septation in *Aspergillus nidulans*. *PLOS ONE* **7**, e31218 (2012).
18. N. Requena, C. Alberti-Segui, E. Winzenburg, C. Horn, M. Schliwa, P. Philippsen, R. Liese, R. Fischer, Genetic evidence for a microtubule-destabilizing effect of conventional kinesin and analysis of its consequences for the control of nuclear distribution in *Aspergillus nidulans*. *Mol. Microbiol.* **42**, 121–132 (2001).
19. J. H. Lenz, I. Schuchardt, A. Straube, G. Steinberg, A dynein loading zone for retrograde endosome motility at microtubule plus-ends. *EMBO J.* **25**, 2275–2286 (2006).
20. J. F. Abenza, A. Pantazopoulou, J. M. Rodríguez, A. Galindo, M. A. Peñalva, Long-distance movement of *Aspergillus nidulans* early endosomes on microtubule tracks. *Traffic* **10**, 57–75 (2009).
21. N. Zekert, R. Fischer, The *Aspergillus nidulans* kinesin-3 UncA motor moves vesicles along a subpopulation of microtubules. *Mol. Biol. Cell* **20**, 673–684 (2009).
22. J. F. Abenza, A. Galindo, A. Pantazopoulou, C. Gil, V. de los Ríos, M. A. Peñalva, *Aspergillus* $RabB^{Rab5}$ integrates acquisition of degradative identity with the long distance movement of early endosomes. *Mol. Biol. Cell* **21**, 2756–2769 (2010).
23. M. Schuster, S. Kilaru, G. Fink, J. Collemare, Y. Roger, G. Steinberg, Kinesin-3 and dynein cooperate in long-range retrograde endosome motility along a nonuniform microtubule array. *Mol. Biol. Cell* **22**, 3645–3657 (2011).
24. L. E. Rogg, J. R. Fortwendel, P. R. Juvvadi, W. J. Steinbach, Regulation of expression, activity and localization of fungal chitin synthases. *Med. Mycol.* **50**, 2–17 (2012).
25. M. D. Lenardon, C. A. Munro, N. A. R. Gow, Chitin synthesis and fungal pathogenesis. *Curr. Opin. Microbiol.* **13**, 416–423 (2010).
26. H. Horiuchi, Functional diversity of chitin synthases of *Aspergillus nidulans* in hyphal growth, conidiophore development and septum formation. *Med. Mycol.* **47**, S47–S52 (2009).
27. K. Fukuda, K. Yamada, K. Deoka, S. Yamashita, A. Ohta, H. Horiuchi, Class III chitin synthase ChsB of *Aspergillus nidulans* localizes at the sites of polarized cell wall synthesis and is required for conidial development. *Eukaryot. Cell* **8**, 945–956 (2009).
28. C. Sacristan, A. Reyes, C. Roncero, Neck compartmentalization as the molecular basis for the different endocytic behaviour of Chs3 during budding or hyperpolarized growth in yeast cells. *Mol. Microbiol.* **83**, 1124–1135 (2012).
29. N. Takeshita, V. Wernet, M. Tsuizaki, N. Grün, H.-o. Hoshi, A. Ohta, R. Fischer, H. Horiuchi, Transportation of *Aspergillus nidulans* class III and V chitin synthases to the hyphal tips depends on conventional kinesin. *PLOS ONE* **10**, e0125937 (2015).
30. J. Wiedenmann, S. Gayda, V. Adam, F. Oswald, K. Nienhaus, D. Bourgeois, G. U. Nienhaus, From EosFP to mIrisFP: Structure-based development of advanced photoactivatable marker proteins of the GFP-family. *J. Biophotonics* **4**, 377–390 (2011).
31. G. U. Nienhaus, K. Nienhaus, A. Hölzle, S. Ivanchenko, F. Renzi, F. Oswald, M. Wolff, F. Schmitt, C. Röcker, B. Vallone, W. Weidemann, R. Heilker, H. Nar, J. Wiedenmann, Photoconvertible fluorescent protein EosFP: Biophysical properties and cell biology applications. *Photochem. Photobiol.* **82**, 351–358 (2006).
32. K. Nienhaus, G. U. Nienhaus, J. Wiedenmann, H. Nar, Structural basis for photo-induced protein cleavage and green-to-red conversion of fluorescent protein EosFP. *Proc. Natl. Acad. Sci. U.S.A.* **102**, 9156–9159 (2005).
33. E. Betzig, G. H. Patterson, R. Sougrat, O. W. Lindwasser, S. Olenych, J. S. Bonifacino, M. W. Davidson, J. Lippincott-Schwartz, H. F. Hess, Imaging intracellular fluorescent proteins at nanometer resolution. *Science* **313**, 1642–1645 (2006).
34. S. T. Hess, T. P. K. Girirajan, M. D. Mason, Ultra-high resolution imaging by fluorescence photoactivation localization microscopy. *Biophys. J.* **91**, 4258–4272 (2006).
35. Y. Li, Y. Ishitsuka, P. N. Hedde, G. U. Nienhaus, Fast and efficient molecule detection in localization-based super-resolution microscopy by parallel adaptive histogram equalization. *ACS Nano* **7**, 5207–5214 (2013).
36. Y. Ishitsuka, N. Savage, Y. Li, A. Bergs, N. Grün, D. Kohler, R. Donnelly, G. U. Nienhaus, R. Fischer, N. Takeshita, Superresolution microscopy reveals a dynamic picture of cell polarity maintenance during directional growth. *Sci. Adv.* **1**, e1500947 (2015).
37. L. Araujo-Bazán, M. A. Peñalva, E. A. Espeso, Preferential localization of the endocytic internalization machinery to hyphal tips underlies polarization of the actin cytoskeleton in *Aspergillus nidulans*. *Mol. Microbiol.* **67**, 891–905 (2008).
38. N. Takeshita, Y. Higashitsuji, S. Konzack, R. Fischer, Apical sterol-rich membranes are essential for localizing cell end markers that determine growth directionality in the filamentous fungus *Aspergillus nidulans*. *Mol. Biol. Cell* **19**, 339–351 (2008).
39. T. Horio, B. R. Oakley, The role of microtubules in rapid hyphal tip growth of *Aspergillus nidulans*. *Mol. Biol. Cell* **16**, 918–926 (2005).
40. A. Berepiki, A. Lichius, N. D. Read, Actin organization and dynamics in filamentous fungi. *Nat. Rev. Microbiol.* **9**, 876–887 (2011).
41. R. López-Franco, S. Bartnicki-Garcia, C. E. Bracker, Pulsed growth of fungal hyphal tips. *Proc. Natl. Acad. Sci. U.S.A.* **91**, 12228–12232 (1994).
42. M. Köhli, V. Galati, K. Boudier, R. W. Roberson, P. Philippsen, Growth-speed-correlated localization of exocyst and polarisome components in growth zones of *Ashbya gossypii* hyphal tips. *J. Cell Sci.* **121**, 3878–3889 (2008).
43. N. Takeshita, M. Evangelinos, L. Zhou, T. Serizawa, R. A. Somera-Fajardo, L. Lu, N. Takaya, G. U. Nienhaus, R. Fischer, Pulses of $Ca^{2+}$ coordinate actin assembly and exocytosis for stepwise cell extension. *Proc. Natl. Acad. Sci. U.S.A.* **114**, 5701–5706 (2017).
44. C. Lin, M. Schuster, S. C. Guimaraes, P. Ashwin, M. Schrader, J. Metz, C. Hacker, S. J. Gurr, G. Steinberg, Active diffusion and microtubule-based transport oppose myosin forces to position organelles in cells. *Nat. Commun.* **7**, 11814 (2016).
45. R. Gibeaux, D. Hoepfner, I. Schlatter, C. Antony, P. Philippsen, Organization of organelles within hyphae of *Ashbya gossypii* revealed by electron tomography. *Eukaryot. Cell* **12**, 1423–1432 (2013).
46. M. E. Tanenbaum, L. A. Gilbert, L. S. Qi, J. S. Weissman, R. D. Vale, A protein-tagging system for signal amplification in gene expression and fluorescence imaging. *Cell* **159**, 635–646 (2014).
47. J. W. Hammond, D. Cai, T. L. Blasius, Z. Li, Y. Jiang, G. T. Jih, E. Meyhofer, K. J. Verhey, Mammalian Kinesin-3 motors are dimeric in vivo and move by processive motility upon release of autoinhibition. *PLOS Biol.* **7**, e1000072 (2009).
48. M. A. Penalva, J. Zhang, X. Xiang, A. Pantazopoulou, Transport of fungal RAB11 secretory vesicles involves myosin-5, dynein/dynactin/p25, and kinesin-1 and is independent of kinesin-3. *Mol. Biol. Cell* **28**, 947–961 (2017).
49. R. Manck, Y. Ishitsuka, S. Herrero, N. Takeshita, G. U. Nienhaus, R. Fischer, Genetic evidence for a microtubule-capture mechanism during polarised growth of *Aspergillus nidulans*. *J. Cell Sci.* **128**, 3569–3582 (2015).
50. N. Takeshita, D. Mania, S. Herrero, Y. Ishitsuka, G. U. Nienhaus, M. Podolski, J. Howard, R. Fischer, The cell-end marker TeaA and the microtubule polymerase AlpA contribute to microtubule guidance at the hyphal tip cortex of *Aspergillus nidulans* to provide polarity maintenance. *J. Cell Sci.* **126**, 5400–5411 (2013).
51. T. Nayak, E. Szewczyk, C. E. Oakley, A. Osmani, L. Ukil, S. L. Murray, M. J. Hynes, S. A. Osmani, B. R. Oakley, A versatile and efficient gene-targeting system for *Aspergillus nidulans*. *Genetics* **172**, 1557–1566 (2006).

**Acknowledgments:** We acknowledge support by Deutsche Forschungsgemeinschaft and Open Access Publishing Fund of Karlsruhe Institute of Technology. **Funding:** This work was supported by the Deutsche Forschungsgemeinschaft (TA819/2-1, FOR1334, NI291/12-1, GRK2039), Helmholtz Association Program STN, Japan Society for the Promotion of Science (JSPS) KAKENHI grant number 15K18663, and Japan Science and Technology Agency (JST) ERATO grant number JPMJER1502. **Author contributions:** G.U.N. and N.T. designed the research project. L.Z., M.E., V.W., and N.T. performed microscopy experiments and analyzed data. M.E., V.W., and N.T. prepared sample strains. L.Z., A.F.E., and Y.I. developed the microscopy analysis. L.Z., R.F., G.U.N., and N.T. wrote the paper with inputs from other coauthors. **Competing interests:** The authors declare that they have no competing interests. **Data and materials availability:** All data needed to evaluate the conclusions in the paper are present in the paper and/or the Supplementary Materials. Additional data related to this paper may be requested from the authors.

Submitted 29 May 2017
Accepted 27 December 2017
Published 24 January 2018
10.1126/sciadv.1701798

**Citation:** L. Zhou, M. Evangelinos, V. Wernet, A. F. Eckert, Y. Ishitsuka, R. Fischer, G. U. Nienhaus, N. Takeshita, Superresolution and pulse-chase imaging reveal the role of vesicle transport in polar growth of fungal cells. *Sci. Adv.* **4**, e1701798 (2018).

# Superresolution and pulse-chase imaging reveal the role of vesicle transport in polar growth of fungal cells

Lu Zhou, Minoas Evangelinos, Valentin Wernet, Antonia F. Eckert, Yuji Ishitsuka, Reinhard Fischer, G. Ulrich Nienhaus and Norio Takeshita

*Sci Adv* **4** (1), e1701798.
DOI: 10.1126/sciadv.1701798